Optics Letters

Wide-field spontaneous Raman spectroscopy imaging system for biological tissue interrogation

K. St-Arnaud,[1,2] K. Aubertin,[1,2] M. Strupler,[1] M. Jermyn,[3,1] K. Petrecca,[3] D. Trudel,[2] and F. Leblond[1,2,*]

[1]Department of Engineering Physics, Polytechnique Montreal, CP 6079, Succ. Centre-Ville, Montreal, Quebec H3C 3A7, Canada
[2]Centre de Recherche du Centre Hospitalier de l'Université de Montréal, 900 rue Saint-Denis, Quebec H2X 0A9, Canada
[3]Department of Neurology and Neurosurgery, Montreal Neurological Institute and Hospital, McGill University, 3801 University St., Montreal, Quebec H3A 2B4, Canada
*Corresponding author: Frederic.leblond@polymtl.ca

Received 1 August 2016; revised 15 September 2016; accepted 16 September 2016; posted 16 September 2016 (Doc. ID 272646); published 5 October 2016

Raman spectroscopy has shown great promise as a method to discriminate between cancerous and normal tissue/cells for a range of oncology applications using microscopy and tissue interrogation instruments such as handheld probes and needles. Here we are presenting preliminary steps toward the development of a practical handheld macroscopic Raman spectroscopy instrument, demonstrating its capabilities to discriminate between different biological tissue types during *ex vivo* porcine experiments. The novel probe design can image a field of view of 25 mm^2 with a spatial resolution <100 μm and an average spectral resolution of 95 cm^{-1}, covering the fingerprint region between 450 to 1750 cm^{-1}. The ability of the system to produce tissue maps based on molecular characteristics is demonstrated using a neural network machine learning technique.

OCIS codes: (170.5660) Raman spectroscopy; (110.4234) Multispectral and hyperspectral imaging; (110.2350) Fiber optics imaging; (170.3880) Medical and biological imaging.

http://dx.doi.org/10.1364/OL.41.004692

For interventional procedures requiring the resection of cancer tissue, patient outcome (survival, quality of life) can be improved by maximizing the volume of cancer resected. Thus, there is a critical need in surgical oncology for portable and accurate tissue characterization tools that can *see* cancer beyond what can currently be detected with standard-of-care medical imaging techniques (e.g., magnetic resonance imaging, computed tomography, nuclear medicine) and minimize the unnecessary removal of healthy tissue to reduce debilitating effects. Optical techniques exploiting the contrast associated with light-tissue interactions are ideal for intraoperative use because of the non-ionizing nature of the interactions, and they can potentially provide high-resolution spectroscopic information to detect the signature of a multitude of molecular species. Several approaches have been developed to guide surgeries following the injection of contrast agents targeting molecular processes associated with specific biomarkers. *In vivo* methods include fluorescence induced by the injection of aminolevulenic acid (ALA), indocyanine green (ICG), and fluorescein [1], but there is a wide range of ongoing research developing targeted fluorescent markers. Another option for surgical guidance is exploiting intrinsic optical contrast of tissue for *in vivo* intraoperative characterization, avoiding the need to administer an exogenous compound and, thus, significantly facilitating clinical translation. Such techniques have been developed for interventional use, including optical coherence tomography to image the attenuation contrast associated with elastic scattering, label-free tissue fluorescence to image intrinsic tissue fluorophores, diffuse reflectance to image the optical contrast associated with tissue chromophores (e.g., haemoglobin, melanin, lipids, water) and elastic scattering, as well as vibrational techniques interrogating tissue based on its fine molecular constituents based on inelastic light scattering [2].

Human tissue is composed of a multitude of molecular species with vibrational properties that can be probed using spontaneous Raman spectroscopy (RS). This technique is thus used for label-free tissue characterization based on molecular fingerprinting in terms of tissue constituents, including lipids, proteins and amino acids, cholesterol, and DNA. Because the concentrations of these biomolecules, as well as their interactions with the cellular/extra-cellular environment, are known to vary between tissue types and pathological status, RS is a promising approach for eventual routine use as an adjunct guidance tool during surgical oncology interventions. Over the past two decades, Raman micro-spectroscopy has been used to detect cancer tissue with high accuracy with *ex vivo* tissue samples and cell cultures for several pathologies [3]. However, only a limited number of studies have been conducted evaluating RS *in vivo* for surgical guidance applications. One of the impediments to the clinical translation of RS for interventional medicine applications includes the difficulty to acquire sufficiently high signal-to-noise ratio (SNR) inelastic scattering within timeframes compatible with the workflow of surgeons. Raman

signals are associated with inelastically scattered light following tissue excitation with a monochromatic laser. Because of the rarity of Raman scattering photons, *in vivo* applications have mostly focused on the development of instruments collecting signals for a limited number of points using small footprint optical probes and needles [4]. Our objective is to move beyond current capabilities associated with single-point detection by developing macroscopic wide-field RS instruments for rapid cancer detection over fields of view as large as several millimeters across with ~100 μm resolution. These length scales are selected because they are consistent with state-of-the-art surgical microscopes and tissue dissection techniques for many applications, including neurosurgery [5].

Here we are presenting preliminary work in the form of a proof-of-principle study that a practical wide-field RS imaging system can be designed using a flexible coherent imaging bundle to image the principal vibrational tissue characteristics associated with proteins and lipids. Only a limited number of wide-field imaging systems have been designed for *in vivo* tissue interrogation with RS. Stimulated Raman spectroscopy was demonstrated *in vivo* for rat brain imaging [6]. However, there remain several challenges before practical optical fiber-based nonlinear signal detection can be used in an operating room [4]. A probe was introduced using spontaneous Raman spectroscopy and mirror displacement at the end of the tip for imaging [7]. However, the incorporation of a spatial scanning setup at the end of the probe makes miniaturization more difficult. Coherent imaging bundles were also used as an optics relay for Raman spectroscopy applications [8,9].

The imaging system (Fig. 1) is composed of a tissue interrogating probe and a hyperspectral imaging camera connected through a 91 cm length flexible coherent imaging fiber optics bundle (Schott, Germany). Tissue illumination is achieved using a 785 nm wavelength-stabilized monochromatic laser (Innovative Photonic Solutions, New Jersey, USA). The excitation light is collimated before passing through a 785 ± 3 nm line filter (Semrock, New York, USA) with subsequent beam expansion, resulting in a circular illumination area of 6 mm diameter in the imaging plane. The light collection probe (proximal end of the imaging bundle) consists of a relay lens in front of which a long-pass filter [>800 nm, optical density (OD) >5] has been placed to block Rayleigh scattering. The relay lens was designed to ensure that the imaging plane is projected onto the entrance plane of the coherent bundle which is composed of a square array of 400 × 400 fibers of 10 μm diameter and has a numerical aperture of 0.6. Light detection is done across a liquid crystal tunable filter (Varispec SNIR LCTF, 650–1100 nm, 7 nm bandwidth) allowing spectral bands to be sequentially selected and imaged with a high-speed EMCCD camera (Hnu, Nuvu; 512 × 512 pixels, 45% quantum efficiency at 850 nm. Another >800 nm long-pass filter is placed in the optical path after the tunable filter to eliminate residual Rayleigh scattering. Objectives are disposed on each side of the tunable filter to ensure that light passing through it is collimated. A full dataset consists of images sequentially acquired for wavelengths between 814 and 910 nm, resulting in one Raman spectrum for each EMCCD pixel. The Raman spectral resolution is limited by the 7 nm bandwidth (95 cm^{-1}) of the tunable filter, resulting in wavenumbers ranging from 453 to 1749 cm^{-1} covering most of the fingerprint region. The field of view (FOV) and the spatial resolution of the system were evaluated using a standard 1951 USAF resolution target. As shown in Fig. 2, the system produces images over a FOV of 25 mm^2 with 55.7 μm spatial resolution. The FOV was determined by imaging the line pairs separated by 2 mm, and the spatial resolution was measured using the Rayleigh criterion.

To evaluate the potential of the wide-field system to distinguish different tissue types, measurements were made on a porcine meat sample, specifically along the *longissimus dorsi* muscle. A sample of approximately 1 cm thickness was purchased from a grocer and kept frozen overnight at 20°C. Measurements were made at an ambient temperature, ensuring that the FOV includes two tissue types (muscle and adipose tissue) separated by a visually detectable frontier (see the photograph in Fig. 3). Each measurement was performed using an integration time of 500 ms per spectral band, resulting in a total imaging time (laser on) <90 s. During each imaging session, the laser was operated at 500 mW and turned off for 150 ms between bands. A dark noise dataset was acquired which consists of a measurement made with the same integration time as for the tissue, but with the laser turned off. Moreover, the instrument response function (IRF) of the system was measured using a 785 nm Raman standard (NIST, Maryland, USA; model SRM2241) for which the luminescence spectrum is known *a priori*. The measurement on the standard material was done using the same laser power and integration time as for tissue imaging.

Post-processing was applied to the raw hyperspectral tissue data using a custom Matlab (MathWorks, Massachusetts, USA) program to isolate the signal component associated with inelastic

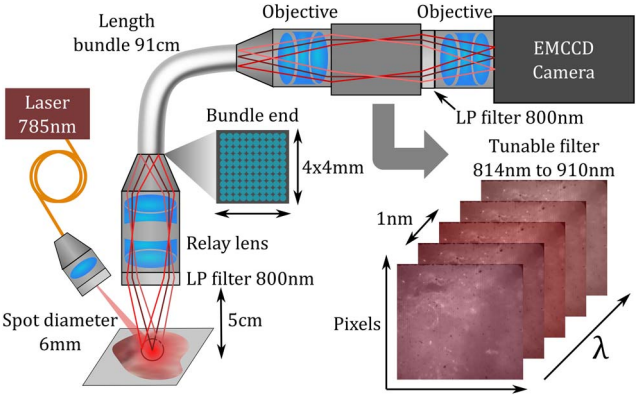

Fig. 1. Schematic depiction of the wide-field spontaneous Raman spectroscopy system.

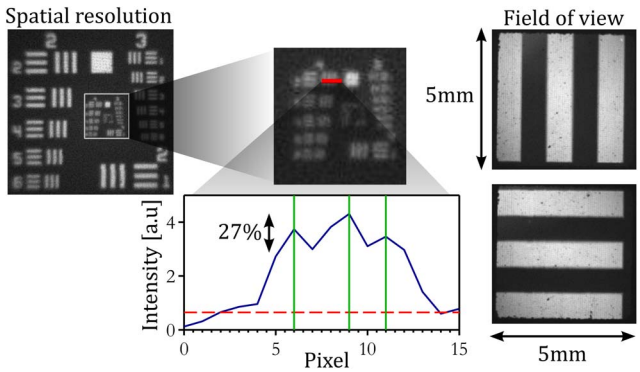

Fig. 2. Measurements made with a standard 1951 USAF resolution target to evaluate the FOV and the spatial resolution of the system.

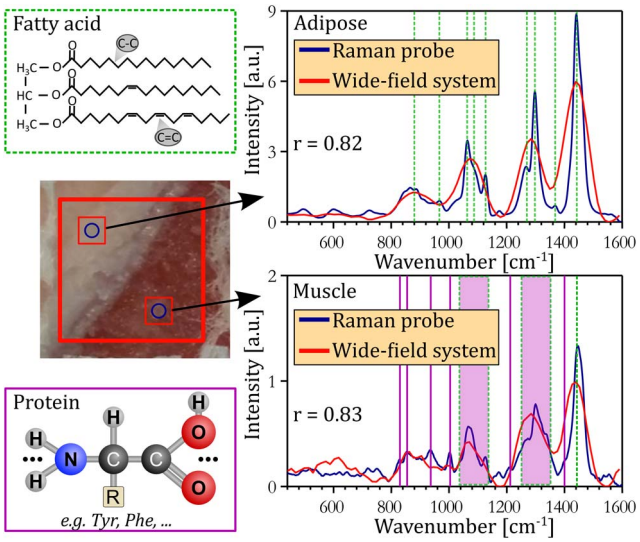

Fig. 3. Direct comparison of the measurements made with the single-point probe and the wide-field Raman spectroscopy system. The larger square in the photograph is the FOV of the imager; the circles are associated with the two tissue areas imagined with the single-point probe that were co-registered with average wide-field spectra acquired within the smaller squares. The spectra for both systems are shown with dotted and plain vertical lines drawn to highlight the characteristics of fatty acid and protein bands, respectively.

scattering. A dark noise measurement was initially subtracted from the tissue imaging dataset followed by a pixel-per-pixel division by the Raman response of the system retrieved from the NIST standard material to remove the IRF and to correct for the nonuniform illumination of the sample. An iterative smoothing function based on a polynomial fit algorithm [10] was then applied to the spectra to evaluate and subtract the contribution from intrinsic tissue fluorescence, and a Savitzky–Golay filter was applied to maximize the removal of non-Raman spectral artifacts. Finally, 4 by 4 spatial binning was applied to maximize the SNR. To verify that the reconstructed spectroscopic features are associated with the expected vibrational tissue characteristics (e.g., amide bands, aromatic amino acid peaks, proteins, and lipid bands), the measurements were made using an established single-point Raman spectroscopy system developed in our laboratory [11]. Single-point measurements were made corresponding to a 0.2 mm^2 area using a 0.2 s total integration time and 60 mW of laser power. Figure 3 shows that single-point probe measurements (circles) were compared with a spectrum averaged over multiple EMCCD pixels in regions of interest (small squares) located within the FOV of the wide-field system (larger square). The raw spectroscopic data collected with the single-point probe were post-processed using a similar procedure as described for the wide-field data.

Spectra were compared (single-point probe versus macroscopic imaging system) for porcine meat measurements in areas associated with muscle and adipose tissue. Single-point probe measurements made on adipose tissue show the distinguishing spectral features associated with the fatty acids [12] represented as dotted vertical lines in Fig. 3. The dominant band at 1438 cm^{-1} is the scissor deformation of CH_2, while the peak associated with the umbrella deformation of CH_3 is seen around 1368 cm^{-1}. Other peaks associated with in-phase twisting of CH_2 and symmetric rock *cis* isomer of =C—H can be observed around 1300 and 1270 cm^{-1}, respectively. The region from 1000 to 1200 cm^{-1} presents three peaks at 1063, 1087, and 1127 cm^{-1}, which are associated with C—C aliphatic stretches. Bands around 967 and 880 cm^{-1} are associated with an out-of-phase bend *cis* isomer of =C—H and C—C stretches. The measurements made on muscle tissue differ from those made on adipose tissue, principally due to higher protein content with relatively fewer lipids [13]. The proteins yield spectral features associated with the backbone of the polypeptide chain (amide bands), the peaks associated with the structure of aromatic amino acids, as well as band characteristics similar to those observed for fatty acids [14]. For example, the large peak between 1220 and 1380 cm^{-1} can be associated with lipids, but also with the amide III band that is usually situated between 1225 and 1305 cm^{-1}. The peaks in the region from 1000 to 1200 cm^{-1} can be associated with a C—C or N stretch of proteins, but also with the presence of lipids. The peaks at 830 and 855 cm^{-1} are associated with tyrosine (Tyr) and the peak at 1004 cm^{-1} is that of phenylalanine (Phe). Although a strong correlation is observed between single-point and wide-field measurements ($r > 0.8$), the limited spectral resolution of the latter thwarts its ability to specifically resolve all spectral features detected with the single-point probe. For example, Fig. 4(b) shows that for adipose tissue the scissor deformation of CH_2 is resolved with the wide-field system, and a second peak is observed representing an average of the 1300 and 1270 cm^{-1} bands. However, the band associated with the umbrella deformation at 1368 cm^{-1} is lost due to its low intensity, but two peaks are observed representing averages over the three C—C aliphatic stretches and averages over the *cis* isomer of =C—H and C—C stretches. Similar conclusions can be reached for muscle tissue but, in this case, the wide-field system also detects a band at 850 cm^{-1} associated with the Tyr peaks and a band around 1005 cm^{-1} that is associated with Phe.

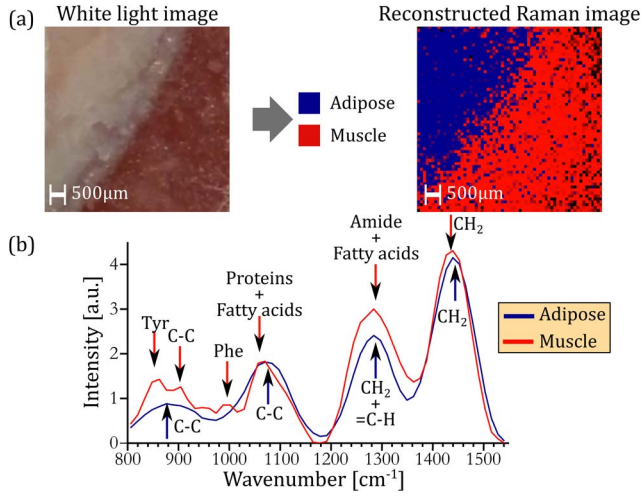

Fig. 4. (a) Image on the left shows a white light photograph of the region imaged with the wide-field system. The image on the right is a false color rendering of the classification result. (b) Representative normalized spectra acquired with the wide-field system for adipose and muscle tissue.

The ability of wide-field RS imaging to automatically distinguish tissue types and produce tissue-specific images was tested using a supervised machine learning technique. To recreate images based on the molecular contrast provided by inelastic scattering, the Matlab neural network classification algorithm was used with 20 hidden neurons. The training dataset consisted of 256 spectra taken over adipose and muscle tissue. To avoid bias, training data were acquired on a different day along the *longissimus dorsi* muscle associated with a different porcine tissue sample. The "tissue type" ground truth was assessed by visual inspection, and 70% of the 256 spectra were used randomly as training data, while the rest were utilized for testing and validation. All spectra were normalized to get a mean of zero and a unitary standard deviation (standard normal variate). This pre-processing was done to ensure classification is more heavily weighted toward spectral rather than intensity differences. The false color image shown in Fig. 4(a) was reconstructed based on the classification result demonstrating that the Raman-based reconstruction reproduces features seen in the white light photograph of the sample. The frontier between adipose and muscle tissue is characterized by a ∼500 μm thick region composed of a mixture of the two tissue types. On the reconstructed images, this region appears as a mixture of both types of tissues since pixels, including infiltrations of a certain tissue type, may be more difficult to classify correctly. The neural network analysis was restricted to the wavenumber region from 800 and 1550 cm^{-1} since, as suggested by Fig. 4(b), most of the tissue information captured by the wide-field system is within that range. The most notable differences between adipose and muscle tissue spectra are associated with the presence of aromatic amino acid peaks in the 800 to 1000 cm^{-1} region. Other differences are associated with the two peaks in the region from 1000 to 1400 cm^{-1}. In adipose tissue, these peaks are only influenced by the fatty acid content while, in muscle tissue, there is also a contribution from proteins. The shape of the peak between 1400 and 1550 cm^{-1} is similar for both adipose and muscle tissue, since it is determined by molecular characteristics similar in both tissue types. However, it was noted on the non-normalized spectra that the intensity of that peak is more prominent in adipose tissue, since it contains much more lipids than muscle tissue.

A proof-of-concept study was presented suggesting wide-field Raman spectroscopy macroscopic tissue imaging could be achieved under experimental conditions compatible with *in vivo* clinical translation for surgical oncology applications. Specifically, we have demonstrated that a frontier between different tissue types (muscle versus adipose tissue) can be detected within ∼1 min with a practical non-contact handheld probe using a flexible imaging bundle. Although the FOV and spatial resolution of the wide-field system are consistent with the intended use for guidance during microsurgical procedures, its usefulness in surgical oncology may be limited by a lack of sensitivity. For example, the computed root-mean-square difference of average single-point probe spectra for adipose versus muscle porcine tissue is 19.4%, whereas it is <4% for normal brain versus glioma [5].

Important characteristics to consider when evaluating system requirements for specific oncology applications include evaluating a minimum per-band Raman SNR, as well as the spectral resolution required to detect tissue peaks important for tissue discrimination. Moreover, some clinical applications will require a larger dynamical range of detection since some tissue types generate high levels of intrinsic fluorescence. For example, the level of auto-fluorescence in prostate tissue can be up to four times larger than in the normal brain. Other system characteristics that may depend on the targeted clinical application include FOV and spatial resolution. For instance, a larger FOV may be advantageous when only gross tumor detection is required, but may be inadequate for applications where cellular infiltrations need to be detected.

Other important factors to consider are imaging time and sensitivity. These parameters can be improved in the actual wide-field system by using a different photodetection strategy. For example, the liquid crystal tunable filter transmits on average <30% of incoming light to an EMCCD with <45% quantum yield for wavelengths >785 nm. Imaging with improved spectral resolution could, for example, be achieved by using a CCD-grating spectroscopic detection system achieving rapid snapshot full-spectra acquisition through line scanning, instead of wavelength scanning, as is the case in Fig. 1. Future work will address those issues through the development of a state-of-the-art handheld imaging device combining Raman illumination with higher sensitivity and spectral resolution.

Funding. Fonds Québécois de la Recherche sur la Nature et les Technologies (FQRNT); Natural Sciences and Engineering Research Council of Canada (NSERC); Canadian Institutes of Health Research (CIHR).

REFERENCES

1. P. A. Valdes, F. Leblond, V. L. Jacobs, K. D. Paulsen, and D. W. Roberts, Curr. Med. Imaging Rev. **8**, 211 (2012).
2. C. Balas, Meas. Sci. Technol. **20**, 104020 (2009).
3. L. A. Austin, S. Osseiran, and C. L. Evans, Analyst **141**, 476 (2016).
4. I. Latka, S. Dochow, C. Krafft, and B. Dietzek, Laser Photon. Rev. **7**, 698 (2013).
5. M. Jermyn, K. Mok, J. Mercier, J. Desroches, J. Pichette, K. Saint-Arnaud, L. Bernstein, M. Guiot, K. Petrecca, and F. Leblond, Sci. Transl. Med. **7**, 274ra19 (2015).
6. M. Ji, D. A. Orringer, C. W. Freudiger, S. Ramkissoon, X. Liu, D. Lau, A. J. Golby, I. Norton, M. Hayashi, N. Y. R. Agar, G. S. Young, C. Spino, S. Santagata, S. Camelo-Piragua, K. L. Ligon, O. Sagher, and X. S. Xie, Sci. Transl. Med. **5**, 201ra119 (2013).
7. H. Sato, T. Tanaka, T. Ikeda, S. Wada, H. Tashiro, and Y. Ozaki, J. Mol. Struct. **598**, 93 (2001).
8. E. Schmälzlin, B. Moralejo, M. Rutowska, A. Monreal-Ibero, C. Sandin, N. Tarcea, J. Popp, and M. M. Roth, Sensors **14**, 21968 (2014).
9. L. V. Doronina-Amitonova, I. V. Fedotov, A. B. Fedotov, and A. M. Zheltikov, Appl. Phys. Lett. **102**, 161113 (2013).
10. J. Zhao, H. Lui, D. I. Mclean, and H. Zeng, Appl. Spectrosc. **61**, 1225 (2007).
11. J. Desroches, M. Jermyn, K. Mok, C. Lemieux-Leduc, J. Mercier, K. St-Arnaud, K. Urmey, M.-C. Guiot, E. Marple, K. Petrecca, and F. Leblond, Biomed. Opt. Express **6**, 2380 (2015).
12. J. R. Beattie, S. E. J. Bell, C. Borgaard, A. Fearon, and B. W. Moss, Lipids **41**, 287 (2006).
13. H. Schmidt, K. Sowoidnich, and H. D. Kronfeldt, Appl. Spectrosc. **64**, 888 (2010).
14. J. R. Beattie, S. E. J. Bell, C. Borggaard, and B. W. Moss, Meat Sci. **80**, 1205 (2008).